

# VTGAN: Semi-supervised Retinal Image Synthesis and Disease Prediction using Vision Transformers

Sharif Amit Kamran,  
University of Nevada, Reno  
skamran@nevada.unr.edu

Khondker Fariha Hossain  
University of Nevada, Reno  
khondkerfariyah@nevada.unr.edu

Alireza Tavakkoli  
University of Nevada, Reno  
tavakkol@unr.edu

Stewart Lee Zuckerbrod  
Houston Eye Associates  
szuckerbrod@houstoneye.com

Kenton M. Sanders  
University of Nevada, Reno  
ksanders@med.unr.edu

Salah A. Baker  
University of Nevada, Reno  
sabubaker@med.unr.edu

## Abstract

*In Fluorescein Angiography (FA), an exogenous dye is injected in the bloodstream to image the vascular structure of the retina. The injected dye can cause adverse reactions such as nausea, vomiting, anaphylactic shock, and even death. In contrast, color fundus imaging is a non-invasive technique used for photographing the retina but does not have sufficient fidelity for capturing its vascular structure. The only non-invasive method for capturing retinal vasculature is optical coherence tomography-angiography (OCTA). However, OCTA equipment is quite expensive, and stable imaging is limited to small areas on the retina. In this paper, we propose a novel conditional generative adversarial network (GAN) capable of simultaneously synthesizing FA images from fundus photographs while predicting retinal degeneration. The proposed system has the benefit of addressing the problem of imaging retinal vasculature in a non-invasive manner as well as predicting the existence of retinal abnormalities. We use a semi-supervised approach to train our GAN using multiple weighted losses on different modalities of data. Our experiments validate that the proposed architecture exceeds recent state-of-the-art generative networks for fundus-to-angiography synthesis. Moreover, our vision transformer-based discriminators generalize quite well on out-of-distribution data sets for retinal disease prediction.*<sup>1</sup>

## 1. Introduction

Fluorescein Angiography (FA) combined with retinal funduscopy is a standard tool for diagnosing various retinal vascular abnormalities and degenerative conditions [40]. In Fluorescein Angiography, a fluorescent fluid is injected into

the blood stream and becomes visible 8 to 10 minutes after insertion. The dosage depends on the viscosity of the dye, age of the patient, and the retina vascular structure [39]. In general, the procedure is safe, but there have been reported cases of allergic reactions, ranging from nausea and vomiting to anaphylactic shock and death [38, 33, 34]. The risk associated with FA signifies the need for non-invasive mechanisms to assess retinal vascular structure.

Various automated systems incorporating image processing and machine learning techniques have been proposed for diagnosing retinal abnormalities and degenerative diseases from fundus photographs [16, 15, 45, 38]. Currently, there are no inexpensive imaging alternative for imaging the vascular structure of the retina. The only alternative for scanning retinal vasculature is via Optical coherence Tomography-Angiography (OCTA) [22]. Although OCTA is capable of mapping the retinal subspace in 3D, the equipment is expensive and its highest resolutions are only achievable on very small areas. Consequently, it is imperative to develop non-invasive and inexpensive techniques for measuring retinal vascular structure to circumvent the inaccessibility and potential risks associated with the existing invasive procedures. The first contribution of this paper is a novel deep learning architecture for producing retinal vascular images (i.e., FA images) from non-invasive fundus photographs.

A major obstacle in using machine learning architectures for ophthalmic applications is the lack of publicly available data – in our work Fluorescein Angiography data [28, 29]. Only a handful of machine learning systems have been proposed to predict disease using FA images. However, these systems are trained and tested on privately held data-sets. Pan *et al.* [43] utilized three such pre-trained architectures on 4067 privately curated images for Abnormal and Normal FA prediction. Similarly, Li *et al.* [36] incorporated the encoder of U-Net [46] for classifying different levels

<sup>1</sup>The code repository can be found in the following [Link](#).

of degradation for 3935 privately held Ultra-widefield FA images. To our knowledge, the only two available public data-sets have only 59 and 70 FA images in total [17, 18]. The second contribution of this paper is a semi-supervised approach in conjunction with a vision transformer architecture to address the challenges in training models that learn pathologies from such small amounts of data.

In particular, we introduce VTGAN, a semi-supervised conditional GAN that can simultaneously produce the retinal vascular structure (i.e. FA images) from fundus photographs, while differentiating between healthy and abnormal retina. The proposed architecture incorporates a novel discriminator based on vision transformers for both patch-level adversarial image detection and image-level disease classification. For qualitative assessment, we compare our proposed architecture with recent state-of-the-art fundus-to-angiogram synthesis architectures [27, 26, 54, 31, 9]. For quantitative evaluation, we use Frechet inception Distance (FID) [21] and Kernel Inception Distance (KID) [1] for quantifying image features and measuring structural similarity. To validate the discriminator’s robustness, we use standard metrics for out-of-distribution classification.

## 2. Related Work

Generative adversarial networks (GAN) have become a staple for image-to-image synthesis [6, 47], inpainting [58, 11] and style transfer [54, 55]. By a combination of multi-scale architectures, these networks can detect and learn fine and coarse features from images [3, 2]. This approach, in turn, can be employed for both conditional [23, 12] and unconditional variants of GAN architectures [5, 57]. Generative networks have also seen success in computer tomography (CT), magnetic resonance imaging (MRI), and X-ray for image segmentation, augmentation and cross-domain information fusion tasks [41, 42, 49, 53].

Recently, GAN models are utilized for synthesizing FA images from fundus photographs [51, 26]. These models employ two generators for coarse and fine image generation. The generators were trained on randomly cropped patches of different scales, while multi-scale discriminators are used to discern local and global features from images. Usually, a discriminator incorporates a linear output for classifying among real or fake (generated) images. In addition, these models utilize the PatchGAN architecture [35] as a discriminator for adversarial and real image classification, by producing the output as a feature map of size  $N \times N$ . Incorporating these ideas, the state-of-the-art models employ an architecture that can retain global information like the shape of optic-disc, contrast, and local features like venular structures, arteries, and microaneurysm [51, 26]. However, the problem with this approach is that the discriminator works on patch-level information. As a result, the cohesive relationship between global and local features

is lost while generating FA from crops of fundus images.

The advent of Vision Transformers (ViT) have improved the performance of state-of-the-art architectures in image classification tasks. The premise of ViT is that image pixels contain inherent spatial coherencies. Therefore, utilizing an image as a sequence of non-overlapping patches and incorporating them into a transformer can better extract intrinsic and spatial features [52]. Unlike image generative pre-trained models such as iGPT [4], which apply transformers to obtain image-level features, ViT works on patch-level features and incorporates their positions by utilizing embedding layers [30, 4].

Vision Transformers retain the cohesiveness of coarse and fine features by utilizing the position of each patch. By mapping this information for  $N \times N$  patches into an  $N \times N$  feature-map, we propose a novel architecture based on vision transformers, called VTGAN and illustrated in Fig. 1. Moreover, we extend VTGAN’s capability by adding a multi layer perceptron (MLP) head for classifying Abnormal and Normal FA images in a semi-supervised manner. This architecture is a significant contribution that addresses training models for FA image classification task based on limited amounts of publicly available data. Qualitative and quantitative evaluations demonstrate that VTGAN surpasses other state-of-the-architectures both in terms of synthesis and classification tasks. Additionally, we demonstrate that the produce FA images by VTGAN are such high quality that expert ophthalmologists cannot reliably identify fake image from real ones.

## 3. Proposed Methodology

This paper proposes a vision-transformer-based generative adversarial network (GAN) consisting of residual, spatial feature aggregation, upsampling and downsampling blocks for generators and transformer encoder blocks for discriminators. For training, perceptual, feature matching, and reconstruction loss is incorporated for generating realistic angiograms from retinal fundus images. First, we discuss coarse and fine generators in section 3.1. We elaborate each distinct blocks in sections 3.2, 3.3, and 3.4. We then elaborate on our newly proposed vision-transformer-based discriminators and their interconnection with the generators to establish the end-to-end generative network in section 3.5. Finally, in section 3.6 we discuss the associated loss functions and their weight multipliers for each distinct architecture that forms the proposed model.

### 3.1. Multi-scale Generators

In order to capture large and fine-scale features to produces realistic vascular images we combine multi-scale coarse and fine generators. We adopt two generators ( $G_{fine}$  and  $G_{coarse}$ ), as illustrated in Fig. 1 in our architecture.  $G_{fine}$  synthesizes local features such as arteries and

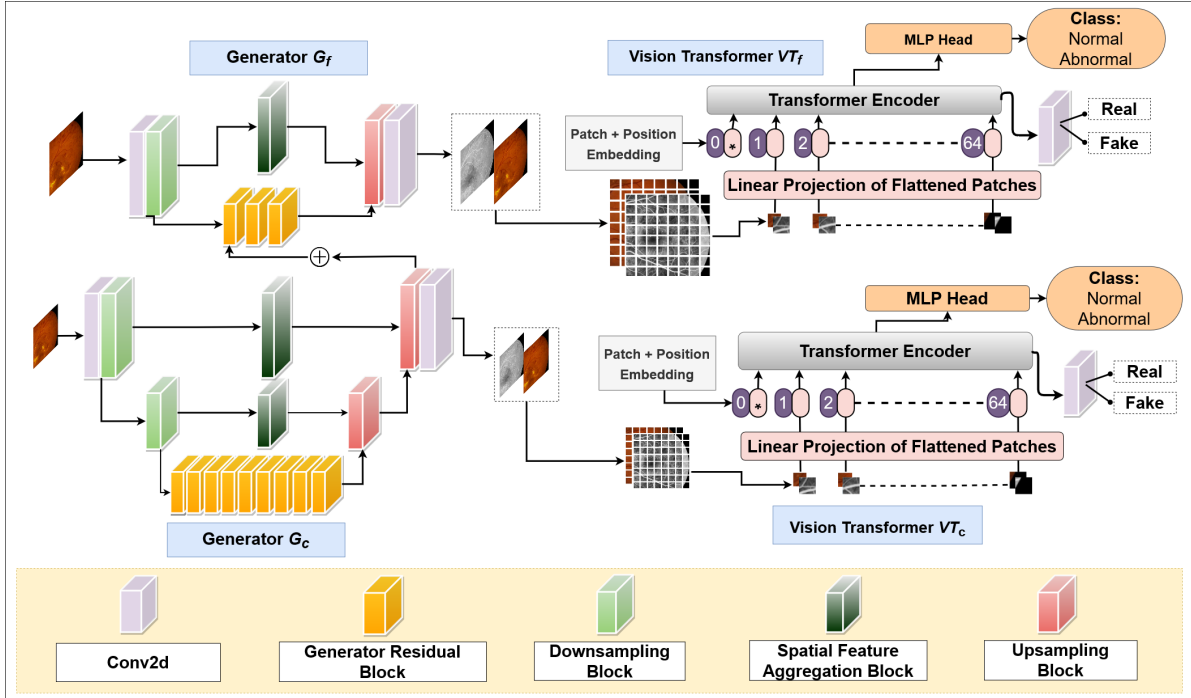


Figure 1. VTGAN consists of Coarse and Fine generators  $G_f, G_c$  and Vision Transformers as discriminators  $VT_f, VT_c$ . The generators take fundus as input and synthesize angiograms. Whereas the vision transformers take patches of the concatenated fundus and angiograms as input and outputs, i) feature-map for adversarial example detection, and ii) image-level classification for Fluorescein angiograms. The generators consist of Downsampling, Upsampling, Spatial Feature Aggregation, and Residual blocks. On the other hand, the Vision transformers consist of Transformer Encoder, Multi-layer perceptron (MLP) head, and adversarial feature output block.

venules. Conversely,  $G_{coarse}$  translates global features such as large blood vessels, optic disc, and overall contrast and illumination. The generators consist of multiple downsampling, upsampling, spatial-aggregation, residual blocks, and a feature summation block between the  $G_{fine}$  and  $G_{coarse}$ . The input and output dimension of  $G_{fine}$  are  $512 \times 512$ , while  $G_{coarse}$  has half the dimension of  $G_{fine}$  ( $256 \times 256$ ). Furthermore, the  $G_{coarse}$  outputs a feature vector of size  $256 \times 256 \times 64$ , which is element-wise added with one of the intermediate layers of the  $G_{fine}$  generator. Both  $G_{coarse}$  and  $G_{fine}$  take fundus images and synthesize FA images. The detailed arrangement is visualized in Fig. 1.

### 3.2. Downsampling and Upsampling Blocks

We use, as generators, auto-encoders comprising of multiple downsampling and upsampling blocks for feature extraction. A single downsampling block contains a convolution layer, a batch-norm layer [24] and a Leaky-ReLU activation function successively and is given in Fig. 2(i). In contrast, an upsampling block consists of a transposed convolution layer, batch-norm [24], and Leaky-ReLU activation layer consecutively and is illustrated in Fig. 2(ii). We use the downsampling block twice in  $G_{coarse}$ , followed by nine successive residual identity blocks. Finally, the upsampling blocks are used  $2 \times$  again to make the spatial output

the same as the input. For  $G_{fine}$ , we utilize the downsampling once, and after three consecutive residual blocks, a single upsampling block is employed to get the same spatial output as the input. We use kernel size,  $k = 3$ , and stride,  $s = 2$  for both of our convolutions and transposed convolution layers.

### 3.3. Generator’s Residual Blocks

For spatial and depth feature extraction, residual blocks have become the fundamental building blocks for image-to-image translation, inpainting, and style transfer tasks [48, 54, 9, 8, 44]. The original residual block consisted of two consecutive convolution layers and a skip connection between the input with the output [19]. Regular convolution operations are computationally inefficient and fail to retain accurate spatial and depth information, unlike separable convolution [10]. Separable convolution incorporates a depth-wise convolution layer followed by a point-wise convolution. Consequently, it obtains and retains depth and spatial features better. We use residual blocks for our generators, as illustrated in Fig. 2(iv). The residual block consists of Reflection padding, Separable Convolution, Batch-Norm, and Leaky-ReLU layers followed by two branches of the same repetitive layers. The main difference is, one branch consists of a dilation rate of  $d = 1$  and the other

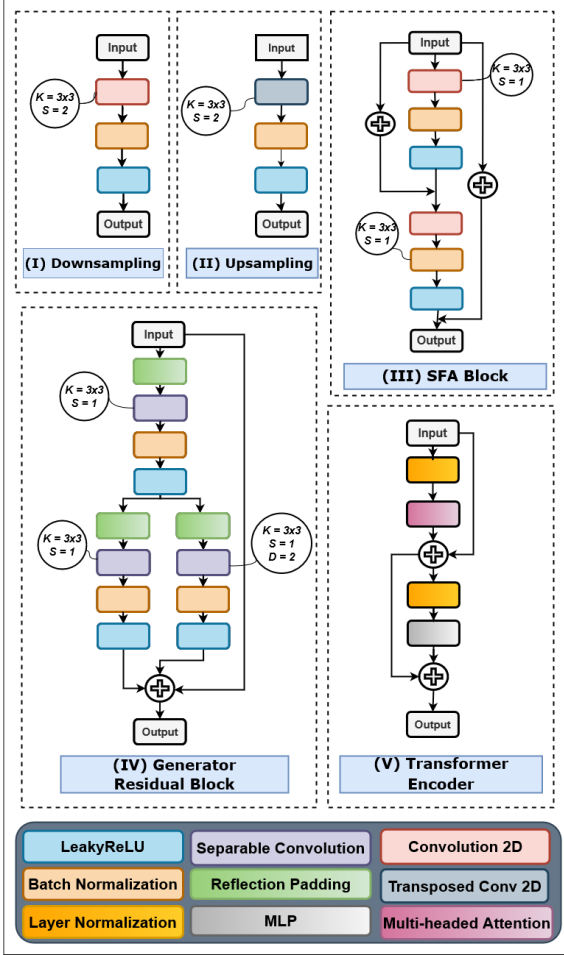


Figure 2. Individual blocks of our proposed GAN architecture consisting of (i) Downsampling, (ii) Upsampling, (c) SFA block, (d) Residual Block for Generator and (e) Transformer Encoder where K stands for kernel size, S is for stride and D is for Dilation rate

with a dilation rate,  $d = 2$  in the separable convolution layers. We use, kernel size,  $k = 3$  and stride,  $s = 1$ . The skip connection and output of the two branches are all element-wise summed in the final output.

### 3.4. Spatial Feature Aggregation Block

In this section, we elaborate on the spatial feature aggregation (SFA) block, as illustrated in Fig. 2(iii). The block consists of two residual units with Convolution, Batch-Norm, Leaky-ReLU layer successively. The convolution layer have kernel,  $k = 3$ , and stride,  $s = 1$ . Additionally, there are two skip connections, one going from the input and element-wise summed to the first residual unit’s output. The next one is coming from the input and being added with the last residual unit’s output. We use spatial feature aggregation block for combining spatial features from the bottom layers with the top layers of the network, as illustrated in Fig. 1.  $G_{coarse}$  consists of two SFA blocks that connect

each of the two downsampling blocks with the two upsampling blocks successively. In contrast,  $G_{fine}$  has only one SFA block between the single downsampling and upsampling block. The reason behind incorporating the SFA block is to extract and retain spatial information that is otherwise lost due to consecutive downsampling and upsampling. As a result, we can combine these features with the learned features of the later layers of the network to get an accurate approximation, as seen in similar GAN architectures [56, 7].

### 3.5. Vision-transformer as Discriminators

GAN discriminators require adapting to local and global information changes for distinguishing between real and fake images. To alleviate this underlying issue, we need a dense network with a large number of computable parameters. Alternatively, convolution with a large receptive field can be employed for obtaining spatial features but can easily lead to overfitting while training the model. To address this issue, we propose a new Vision Transformer-based Markovian discriminator, in the same vein as PatchGAN [35]. We use eight vision transformer encoders consisting of a multi-headed attention layer and multi-layer perceptron (MLP) block. The Layer Normalization layer precedes each block, and residual skip connection is added to the output from the input. The block is visualized in Fig. 2(v). To handle 2D images of  $512 \times 512$ , we reshape the images into a sequence of flattened 2D patches with resolution  $64 \times 64$ . By doing so, we end up having 64 patches in total. The Transformer uses a constant latent vector size of  $D = 64$  through all of its layers, so we flatten the patches and map to  $D$  dimensions with a trainable linear projection. The output of this projection is called the patch embeddings as mentioned in [13]. Position embeddings are added to the patch embeddings to preserve positional information. We use regular learnable 1D position embeddings in a similar manner to Dosovitskiy *et al.* [13]. For multi-headed attention, we use  $n = 4$  heads. For MLP blocks, we use two dense layers with features size  $h = [128, 64]$ , each succeeded by a GeLU activation [20] and a dropout of 0.1. Contrarily, our vision transformer has two outputs, an MLP head, and a Convolutional layer, as illustrated in Fig. 1. The MLP head has two output hidden units for FA image classification (Abnormal and Normal). In contrast, the convolution layer outputs a feature map of  $64 \times 64$  for classifying each patch in the original image as Real or Fake.

We use two vision transformer-based discriminators that incorporate identical structures but operate at two different scales. We term the two discriminators as,  $VT_{fine}$  and  $VT_{coarse}$  as illustrated in Fig. 1. We resize the coarse angiograms and fundus with size  $256 \times 256$  by a factor of 2 using the Lanczos filter [14]. Both discriminators have identical transformer encoder and output layers (in Fig. 2(v)).

$VT_{coarse}$  tries to convince the coarse generator,  $G_{coarse}$  to retain more global features such as the macula, optic disc, contrast, and illumination. On the other hand, the  $VT_{fine}$  steers the fine generator,  $G_{fine}$  to synthesize more accurate local features such as small vasculature, venules, exudates, arteries. Consequently, we fuse learnable elements from both generators while training them separately with their paired vision transformer-based discriminators.

### 3.6. Weighted Cost Functions and Adversarial Loss

With the given discriminators and generators, our whole network’s objective function can be formulated as Eq. 1. It’s a multi-objective problem of maximizing the discriminators’ loss while minimizing the generator’s loss.

$$\min_{G_f, G_c} \max_{D_f, D_c} \mathcal{L}_{adv}(G_f, G_c, D_f, D_c) \quad (1)$$

For adversarial training, we use Hinge-Loss [56, 37] as illustrated in Eq. 2 and Eq. 3. All the fundus images and their corresponding angiogram pairs are normalized to  $[-1, 1]$ , and we employ  $\tanh$  as the output activation for the adversarial feature-map. In Eq. 4 we add them and use  $\lambda_{adv}$  as weight multiplier with the  $\mathcal{L}_{adv}(G)$ . For classification we use  $\text{softmax}$  activation after the MLP head output. In Eq. 5 the categorical cross-entropy loss is given where  $y$  is the real class and  $\hat{y}$  is the predicted class.

$$\mathcal{L}_{adv}(D) = -\mathbb{E}_{x,y} [\min(0, -1 + D(x, y))] - \mathbb{E}_x [\min(0, -1 - D(x, G(x)))] \quad (2)$$

$$\mathcal{L}_{adv}(G) = -\mathbb{E}_{x,y} [(D(G(x), y))] \quad (3)$$

$$\mathcal{L}_{adv}(G, D) = \mathcal{L}_{adv}(D) + \lambda_{adv}(\mathcal{L}_{adv}(G)) \quad (4)$$

$$\mathcal{L}_{cce}(D) = \mathbb{E}_{y,\hat{y}} \left[ -\sum_{i=1}^k y_i \log \hat{y}_i \right] \quad (5)$$

Here, In Eq. 2 and Eq. 3 the discriminators are first trained on the real fundus,  $x$  and real angiogram,  $y$ , and then trained on the real fundus,  $x$  and synthesized angiogram,  $G(x)$ . We begin by batch-wise training the discriminators  $D_f$  and  $D_c$  for a couple of iterations on randomly sampled data. After that, we train the  $G_c$  while keeping the weights of the discriminators frozen. Similarly, we train the  $G_f$  on a batch of random images while keeping the weights of all the discriminators frozen.

The generators also incorporate the reconstruction and perceptual loss [25] as shown in Eq. 6 and Eq. 7. We ensure the synthesized images retain more realistic color, contrast, and vascular structure by employing these losses. We also incorporate feature matching loss [54] with all our discriminators and is given in Eq. 8.

$$\mathcal{L}_{rec}(G) = \mathbb{E}_{x,y} \|G(x) - y\|^2 \quad (6)$$

$$\mathcal{L}_{perc}(G) = \mathbb{E}_{x,y} \sum_{i=1}^k \frac{1}{M} \|F_{vgg}^i(y) - F_{vgg}^i(G(x))\| \quad (7)$$

$$\mathcal{L}_{fm}(G, D_n) = \mathbb{E}_{x,y} \sum_{i=1}^k \frac{1}{N} \|D_n^i(x, y) - D_n^i(x, G(x))\| \quad (8)$$

For Eq. 6,  $\mathcal{L}_{rec}$  is the reconstruction loss for the real angiogram,  $y$ , given a generated angiogram,  $G(x)$ . We use this loss for both  $G_f$  and  $G_c$  so that the model can generate high-quality angiograms of different scales. In Eq. 7,  $\mathcal{L}_{perc}$  calculates the difference between real and fake angiogram features extracted by pushing both of them successively in VGG19 architecture [50]. Lastly, Eq. 8 is calculated by taking the features from intermediate layers of the discriminator by first inserting the real and fake angiograms consecutively. Here,  $M$  and  $N$  stand for the number of feature layers extracted from VGG19 and the discriminators consecutively.

By incorporating Eq. 4, 5, 6, 7 and 8 we can formulate our final objective function as given in Eq. 9.

$$\min_{G_f, G_c} \left( \max_{D_f, D_c} (\mathcal{L}_{adv}(G_f, G_c, D_f, D_c)) + \lambda_{rec} [\mathcal{L}_{rec}(G_f, G_c)] + \lambda_{fm} [\mathcal{L}_{fm}(G_f, G_c, D_f, D_c)] + \lambda_{perc} [\mathcal{L}_{perc}(G_f, G_c)] + \lambda_{cce} [\mathcal{L}_{cce}(D_f, D_c)] \right) \quad (9)$$

Here,  $\lambda_{adv}$ ,  $\lambda_{rec}$ ,  $\lambda_{perc}$ ,  $\lambda_{fm}$  and  $\lambda_{cce}$  signify loss weights, and dictate which networks to prioritize while training. For our architecture, more weight is given to the  $\mathcal{L}_{adv}(G)$ ,  $\mathcal{L}_{rec}$ ,  $\mathcal{L}_{perc}$ ,  $\mathcal{L}_{cce}$ , and thus we select bigger  $\lambda$  values for those.

## 4. Experiments

The following section describes our model’s experiments and evaluates our architecture based on qualitative and quantitative metrics. First, we discuss the pre-processing pipeline for our dataset in Sec. 4.1. Next, we detail our hyper-parameter selection and tuning in Sec. 4.2. Also, we compare our architecture with existing state-of-the-art generative models based on some qualitative evaluation metrics in Sec. 4.3. Lastly, in Sec. 4.4 and Sec. 4.5, we analyze the quantification done by experts and the performance on the out-of-distribution dataset.

### 4.1. Dataset

We use the fundus and angiography dataset provided in [17]. The dataset contains thirty images and twenty-nine pairs of the healthy and unhealthy fundus and angiogram images. Each image pair is collected from individual patients. After close observation, we found seventeen images based on one-to-one alignment between the fundus and angiogram pairs. These image pairs are either accurately aligned or almost aligned. The original image size is

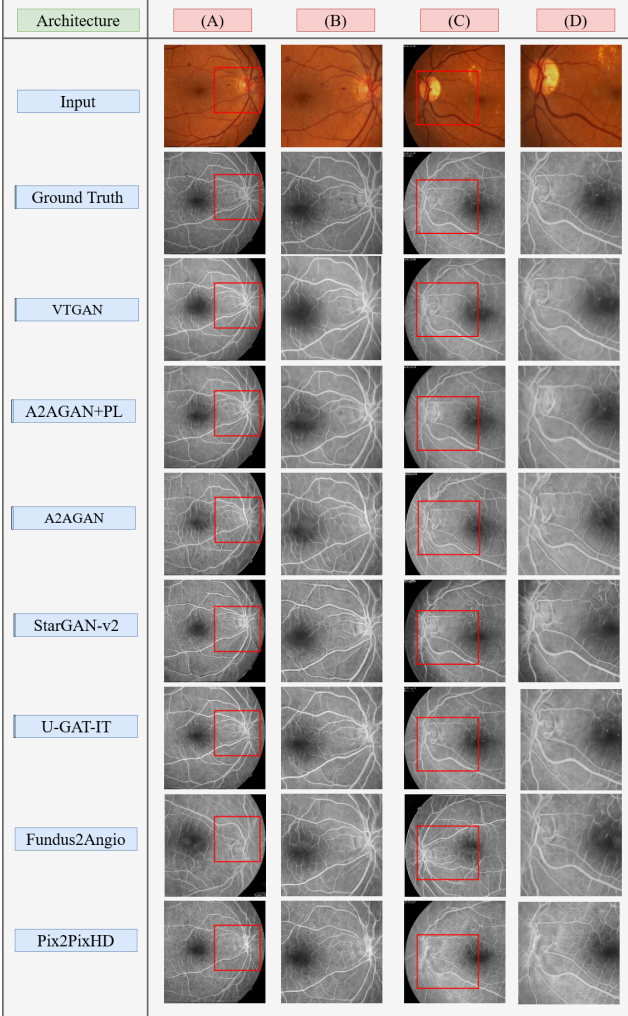


Figure 3. Comparativie results of different Angiograms generated using different state-of-the-art architectures. Column (A) and (C) represents two samples of real fundus, real angio and predicted angio images. Whereas column (B) and (D) represents the red rectangle box to show zoomed in local venular structures corresponding.

$576 \times 720$ , but we take 50 overlapping crops of  $512 \times 512$  sized samples from each. For the image synthesis task, we end up having 850 images in total for training. The fundus images are in RGB format, and angiograms are in a Gray-scale format. As the dataset is categorized into Abnormal and Normal classes, we use this annotation for our supervised classification training. Out of seventeen images, ten are Abnormal, and seven are Normal patients. Due to cropping, we end up having 500 for abnormal and 350 for normal images. We use data augmentation to increase the sample size the same as the abnormal one. For testing, we take fourteen image pairs and crop four overlapping quadrants of the image to generate a set of fifty-six images and use their associated labels.

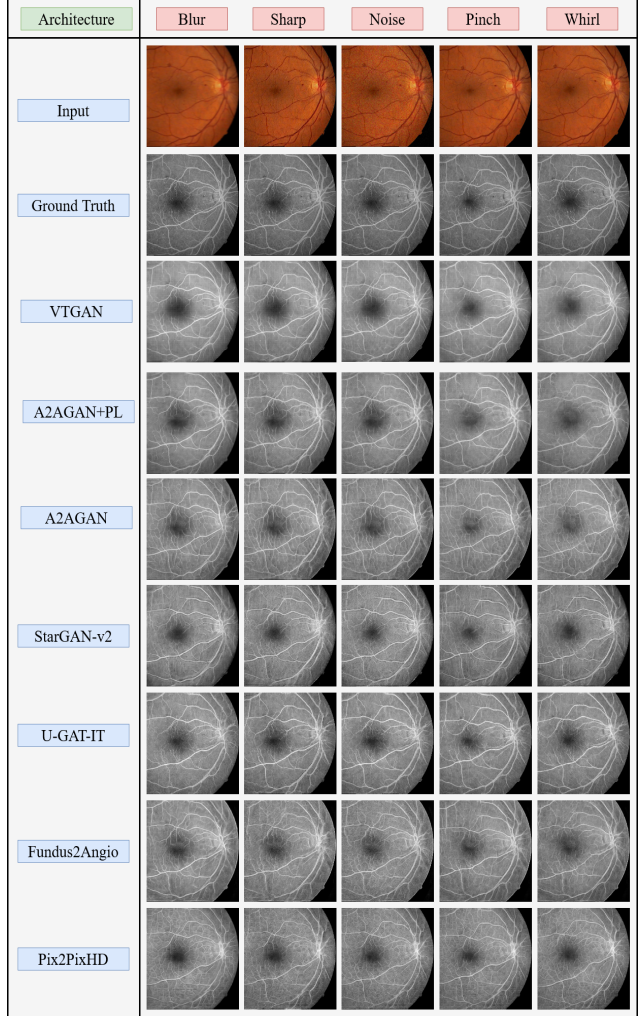


Figure 4. Angiogram generated from transformed and distorted Fundus images with natural changes, imaging errors and biological markers.

## 4.2. Hyper-parameter tuning

For adversarial training, we used hinge loss [56, 37]. We picked  $\lambda_{adv} = 10$  (Eq. 4) and  $\lambda_{rec} = 10$ ,  $\lambda_{perc} = 10$ ,  $\lambda_{fm} = 1$ ,  $\lambda_{cce} = 10$  (Eq. 9). We use Adam optimizer [32], with learning rate  $\alpha = 0.0002$ ,  $\beta_1 = 0.5$  and  $\beta_2 = 0.999$ . We train with mini-batches with batch size,  $b = 2$  for 200 epochs for 50 hours with NVIDIA P100 GPUs.

## 4.3. Qualitative Evaluation

For evaluating our architecture’s performance, we used 14 test samples and cropped four quadrants of the image with a resolution of  $512 \times 512$ . We conducted two experiments for estimating the accurate visual representation i) without transformation and ii) with spatial and radial transformations. By doing so, we measured the network’s ability to adjust to structural changes due to imaging error and pa-

Table 1. Test results for different architectures

Fréchet Inception Distance (FID)						
Architecture	Orig.	Noise	Blur	Sharp	Whirl	Pinch
<b>VTGAN</b>	<b>17.3</b>	<b>18.7</b> (1.4 $\uparrow$ )	24.1 (6.8 $\uparrow$ )	<b>24.5</b> (7.2 $\uparrow$ )	28.4 (11.1 $\uparrow$ )	<b>22.3</b> (5.0 $\uparrow$ )
A2AGAN w/ PL <sup>1</sup> [26]	24.6	21.6 (3.0 $\downarrow$ )	30.0 (5.4 $\uparrow$ )	25.6 (1.0 $\uparrow$ )	40.0 (15.4 $\uparrow$ )	24.9 (0.3 $\uparrow$ )
A2AGAN [26]	20.7	20.8 (0.1 $\uparrow$ )	<b>23.5</b> (2.8 $\uparrow$ )	24.9 (4.2 $\uparrow$ )	<b>27.8</b> (7.1 $\uparrow$ )	19.5 (1.2 $\downarrow$ )
StarGAN-v2 [9]	27.7	35.1 (7.4 $\uparrow$ )	32.6 (4.9 $\uparrow$ )	27.4 (0.3 $\downarrow$ )	32.7 (5.0 $\uparrow$ )	26.7 (1.0 $\downarrow$ )
U-GAT-IT [31]	24.5	26.0 (1.5 $\uparrow$ )	30.4 (5.9 $\uparrow$ )	26.8 (2.3 $\uparrow$ )	33.0 (9.5 $\uparrow$ )	29.1 (4.6 $\uparrow$ )
Fundus2Angio [27]	30.3	41.5 (11.2 $\uparrow$ )	32.3 (2.0 $\uparrow$ )	34.3 (4.0 $\uparrow$ )	38.2 (7.9 $\uparrow$ )	33.1 (2.8 $\uparrow$ )
Pix2PixHD [54]	42.8	53.0 (10.2 $\uparrow$ )	43.7 (1.1 $\uparrow$ )	47.5 (4.7 $\uparrow$ )	45.9 (3.1 $\uparrow$ )	39.2 (3.6 $\downarrow$ )
Kernel Inception Distance (KID)						
Architecture	Orig.	Noise	Blur	Sharp	Whirl	Pinch
<b>VTGAN</b>	<b>0.00053</b>	<b>0.04953</b>	<b>0.00205</b>	<b>0.04927</b>	<b>0.04815</b>	<b>0.04542</b>
A2AGAN w/ PL <sup>1</sup> [26]	0.00087	0.05045	0.00235	0.05162	0.05390	0.04575
A2AGAN [26]	0.00392	0.05390	0.00505	0.05301	0.05657	0.05341
StarGAN-v2 [9]	0.00118	0.05274	0.00235	0.05331	0.05539	0.05271
U-GAT-IT [31]	0.00131	0.05610	0.00278	0.05533	0.05815	0.05719
Fundus2Angio [27]	0.00184	0.05328	0.00272	0.05267	0.05278	0.04985
Pix2PixHD [54]	0.00258	0.05613	0.00254	0.05788	0.06029	0.05838

<sup>1</sup> PL = Perceptual Loss

<sup>2</sup> FID: Lower is better; KID: Lower is better

tient eye movements.

For our first experiment, we compare our network with other state-of-the-art image-to-image translation architectures. A side-by-side comparison of the results is visualized in Fig. 3. Column, A & C in Fig. 3, display the global feature differences while column B & D are zoomed-in local vasculature changes. By its looks, our model produces vivid and convincing results compared to other architectures. Attention2Angio (A2AGAN) and U-GAT-IT also yield impressive results. However, if observed for the closed-up versions in columns B & D, we can witness that the optic disc contains fewer blood vessels. StarGAN-v2 and Pix2PixHD also fail to generate rich arteries, exudates, and vasculature.

In the second set of experiments, we applied three transformations and two distortions on the fundus images: 1) Blur to represent severe cataracts, 2) Sharpening to represent dilated pupils, 3) Noise to sensor impedance during funduscopy, 4) Pinch to visualize squinting as a vascular change, and, 5) Whirl, for distortions caused by increased intraocular pressure (IOP). We can see in Fig. 4 a side-by-side comparison of different architecture predictions on these transformed images. As observed from the results, VTGAN synthesizes images very similar to the ground-truth (GT) and performs robustly to preserve the vascular structures.

For **Blurred** fundus images, VTGAN is less impacted by the transformation compared to other state-of-the-art architecture, as seen in (row 4 to 9 of column 1) of Fig. 4. The vascular structures are better retained as opposed to U-GAT-IT and Fundus2Angio. For **Sharpened** fundus, the angiogram generated by StarGAN-v2 and A2AGAN (row 4

to 6 of column 2) exhibits small artifacts around the blood vessels not present in our case. For **Noisy** images, our result is unaffected by this pixel-level alteration. However, all other state-of-the-art models (row 4 to 9 of column 3) fail to synthesize tiny and slim venular branches.

For **Pinch** and **Whirl**, our experimental result shows the versatility and reproducibility of VTGAN for retaining vascular structure and is illustrated in Fig. 4 (row 3 of column 4 and 5). Compared to ours, only A2AGAN and U-GAT-IT reserves the flattening condition and manifestation of vascular changes but loses the overall smoothness in the process (row 5 to 7 of columns 4 and 5). In Fig. 4 VTGAN encodes the vascular feature information and is much less affected by both kinds of warping. The other architectures failed to generate microvessels due to IOP or vitreous variations, as can be seen in Fig. 4. Consequently, For all kinds of transformation and contortion, VTGAN surpasses existing state-of-the-art image-to-image translation models.

#### 4.4. Quantitative Evaluations

For quantitative evaluation, we performed two experiments. In the first experiment, we use the Fréchet inception distance (FID) [21], and Kernel Inception distance (KID) [1] which has been previously employed for measuring similar image-to-image translation GANs [9, 31]. We computed the FID and KID scores for different architectures on the generated FA image and original angiogram, including the five spatial and radial transformations. The results are given in Table. 4.2. A lower FID and KID score means the synthesized images are more close to the real angiogram.

From Table. 4.2, out of our three networks, the best KID

Table 2. Results of Qualitative with Undisclosed Portion of Fake/Real Experiment

Architecture		Results		Average		
		Correct	Incorrect	Missed <sup>1</sup>	Found <sup>1</sup>	Precision <sup>2</sup>
VTGAN	Fake	6%	94%	57%	43%	<b>45.9%</b>
	Real	80%	20%			

<sup>1</sup> Missed higher is better; Found lower is better

<sup>2</sup> Precision Lower is better

is achieved for VTGAN. And it reaches the lowest scores out of all other architecture, for both with and without distortions. For FID, our model achieves the lowest score for three out of five types of distortions. Attention2Angio scores lower FID for Blur and Whirl transformation.

In the second experiment, we assess the generated angiogram’s quality by asking two expert ophthalmologists to identify them. We use a balanced set of 50 images, 25 real and 25 fake. We then shuffle the data before the expert evaluation. For this experiment, experts did not know the exact number of fake and real images. By not disclosing this, we tried to estimate the following criterion: 1) Correct fake and real angiograms found by the experts, where lower equates to better, 2) Incorrect fake and real angiograms missed by the experts, where higher equates to better, and 3) The average precision of the experts for identifying fake angiograms, where lower equates to better. Table 2 illustrates the detailed result.

As it can be seen from Table 2, experts assigned 94% of the fake angiograms as real, for images synthesized by our models. The result also shows that experts had trouble identifying fake images, while they easily identified real angiograms with 80% certainty. On average, the experts misclassified 57% of all images produced by VTGAN. The average precision diagnosis of the experts are 45.9%. Consequently, our model successfully fools the experts to identify fake angios as real.

#### 4.5. Disease Classification

For our subsequent experimentation, we test our visual transformer’s accuracy on in-distribution and out-of-distribution classification tasks. We use data provided by Hajeb *et al.* [17]. We crop four quadrants from the 14 Fundus and Angiogram pairs because of the shortage of data. Out of 56 images, 20 are for Abnormal, and 36 are for Normal classes. We name this test set as in-distribution and measure the performance using three standard metrics: Accuracy, Sensitivity, and Specificity. The result is provided in Table. 3, and our vision transformer-based model scores

Table 3. Test Accuracy on in-distribution Abnormal/Normal Angiograms

Accuracy	Sensitivity	Specificity
85.7	83.3	90.0

Table 4. Test Accuracy on out-of-distribution Abnormal/Normal Angiograms

Distortion	Accuracy	Sensitivity	Specificity
Blur	78.6 (7.1 ↓)	72.2 (11.1 ↓)	90.0 (-)
Sharp	76.7 (8.0 ↓)	69.4 (13.9 ↓)	90.0 (-)
Noise	78.6 (7.1 ↓)	72.2 (11.1 ↓)	90.0 (-)
Pinch	78.6 (7.1 ↓)	72.2 (11.1 ↓)	90.0 (-)
Whirl	78.6 (7.1 ↓)	72.2 (11.1 ↓)	90.0 (-)

85.7%, 83.3%, 90% for accuracy, sensitivity, and specificity successively.

We use spatial and radial transformation on test images for out-of-distribution evaluation. The model’s performance is illustrated in Table. 4. As can be seen from the table, for Blur, Noise, Pinch, and Whirl transformations, the Accuracy and Sensitivity decreased to 78.6%, 72.2%, consecutively. Compared to the in-distribution data, the decrease is 7.1%, 11.1% for Accuracy and Sensitivity. For Sharp transformation, the accuracy and sensitivity are worse than the other distortions. They are 76.7%, 69.4% successively. An interesting revelation is the specificity has no effect due to these distortions. The specificity is firm 90.0% for all five distortions. A higher specificity signifies our model accurately predicts Abnormal classes better compared to Normal ones. This is significant, as we want to identify patients with degenerative conditions compared to predicting false positives for healthy patients.

## 5. Conclusion

In this paper, we proposed a new fundus-to-angiogram translation architecture called VTGAN. The architecture generates realistic angiograms from fundus images without any expert intervention. Additionally, we provided results for its robustness and adaptability conditioned upon radial and spatial transformations, which imitate biological markers seen in real fundus images. We believe the proposed network can be incorporated in the wild to generate precise FA images of patients developing disease overtime. It can be a complimentary disease progression monitoring system for predicting the development of diseases in vivo. We hope to extend this work to other areas of ophthalmological image modalities.

## References

- [1] Mikołaj Bińkowski, Dougal J Sutherland, Michael Arbel, and Arthur Gretton. Demystifying mmd gans. *arXiv preprint arXiv:1801.01401*, 2018. 2, 7
- [2] Matthew Brown, David G Lowe, et al. Recognising panoramas. In *ICCV*, volume 3, page 1218, 2003. 2
- [3] Peter Burt and Edward Adelson. The laplacian pyramid as a compact image code. *IEEE Transactions on communications*, 31(4):532–540, 1983. 2



- [4] Mark Chen, Alec Radford, Rewon Child, Jeffrey Wu, Heewoo Jun, David Luan, and Ilya Sutskever. Generative pre-training from pixels. In *International Conference on Machine Learning*, pages 1691–1703. PMLR, 2020. 2
- [5] Qifeng Chen and Vladlen Koltun. Photographic image synthesis with cascaded refinement networks. In *Proceedings of the IEEE international conference on computer vision*, pages 1511–1520, 2017. 2
- [6] Wengling Chen and James Hays. Sketchygan: Towards diverse and realistic sketch to image synthesis. In *Proceedings of the IEEE Conference on Computer Vision and Pattern Recognition*, pages 9416–9425, 2018. 2
- [7] Xinyuan Chen, Chang Xu, Xiaokang Yang, and Dacheng Tao. Attention-gan for object transfiguration in wild images. In *Proceedings of the European Conference on Computer Vision (ECCV)*, pages 164–180, 2018. 4
- [8] Yunjey Choi, Minje Choi, Munyoung Kim, Jung-Woo Ha, Sunghun Kim, and Jaegul Choo. Stargan: Unified generative adversarial networks for multi-domain image-to-image translation. In *Proceedings of the IEEE conference on computer vision and pattern recognition*, pages 8789–8797, 2018. 3
- [9] Yunjey Choi, Youngjung Uh, Jaejun Yoo, and Jung-Woo Ha. Stargan v2: Diverse image synthesis for multiple domains. In *Proceedings of the IEEE/CVF Conference on Computer Vision and Pattern Recognition*, pages 8188–8197, 2020. 2, 3, 7
- [10] François Chollet. Xception: Deep learning with depthwise separable convolutions. In *Proceedings of the IEEE conference on computer vision and pattern recognition*, pages 1251–1258, 2017. 3
- [11] Tali Dekel, Chuhan Gan, Dilip Krishnan, Ce Liu, and William T Freeman. Sparse, smart contours to represent and edit images. In *Proceedings of the IEEE Conference on Computer Vision and Pattern Recognition*, pages 3511–3520, 2018. 2
- [12] Emily L Denton, Soumith Chintala, Rob Fergus, et al. Deep generative image models using a laplacian pyramid of adversarial networks. In *Advances in neural information processing systems*, pages 1486–1494, 2015. 2
- [13] Alexey Dosovitskiy, Lucas Beyer, Alexander Kolesnikov, Dirk Weissenborn, Xiaohua Zhai, Thomas Unterthiner, Mostafa Dehghani, Matthias Minderer, Georg Heigold, Sylvain Gelly, et al. An image is worth 16x16 words: Transformers for image recognition at scale. *arXiv preprint arXiv:2010.11929*, 2020. 4
- [14] Claude E Duchon. Lanczos filtering in one and two dimensions. *Journal of applied meteorology*, 18(8):1016–1022, 1979. 4
- [15] Huazhu Fu, Jun Cheng, Yanwu Xu, Changqing Zhang, Damon Wing Kee Wong, Jiang Liu, and Xiaochun Cao. Disc-aware ensemble network for glaucoma screening from fundus image. *IEEE transactions on medical imaging*, 37(11):2493–2501, 2018. 1
- [16] Nikita Gurudath, Mehmet Celenk, and H Bryan Riley. Machine learning identification of diabetic retinopathy from fundus images. In *2014 IEEE Signal Processing in Medicine and Biology Symposium (SPMB)*, pages 1–7. IEEE, 2014. 1
- [17] Shirin Hajeb Mohammad Alipour, Hossein Rabbani, and Mohammad Reza Akhlaghi. Diabetic retinopathy grading by digital curvelet transform. *Computational and mathematical methods in medicine*, 2012, 2012. 2, 5, 8
- [18] Shirin Hajeb Mohammad Alipour, Hossein Rabbani, and Mohammadreza Akhlaghi. A new combined method based on curvelet transform and morphological operators for automatic detection of foveal avascular zone. *Signal, Image and Video Processing*, 8(2):205–222, 2014. 2
- [19] Kaiming He, Xiangyu Zhang, Shaoqing Ren, and Jian Sun. Deep residual learning for image recognition. In *Proceedings of the IEEE conference on computer vision and pattern recognition*, pages 770–778, 2016. 3
- [20] Dan Hendrycks and Kevin Gimpel. Gaussian error linear units (gelus). *arXiv preprint arXiv:1606.08415*, 2016. 4
- [21] Martin Heusel, Hubert Ramsauer, Thomas Unterthiner, Bernhard Nessler, and Sepp Hochreiter. Gans trained by a two time-scale update rule converge to a local nash equilibrium. In *Advances in neural information processing systems*, pages 6626–6637, 2017. 2, 7
- [22] David Huang, Eric A Swanson, Charles P Lin, Joel S Schuman, William G Stinson, Warren Chang, Michael R Hee, Thomas Flotte, Kenton Gregory, Carmen A Puliafito, et al. Optical coherence tomography. *science*, 254(5035):1178–1181, 1991. 1
- [23] Xun Huang, Yixuan Li, Omid Poursaeed, John Hopcroft, and Serge Belongie. Stacked generative adversarial networks. In *Proceedings of the IEEE conference on computer vision and pattern recognition*, pages 5077–5086, 2017. 2
- [24] Sergey Ioffe and Christian Szegedy. Batch normalization: Accelerating deep network training by reducing internal covariate shift. *arXiv preprint arXiv:1502.03167*, 2015. 3
- [25] Justin Johnson, Alexandre Alahi, and Li Fei-Fei. Perceptual losses for real-time style transfer and super-resolution. In *European conference on computer vision*, pages 694–711. Springer, 2016. 5
- [26] Sharif Amit Kamran, Khondker Fariha Hossain, Alireza Tavakkoli, and Stewart Lee Zuckerbrod. Attention2angiogan: Synthesizing fluorescein angiography from retinal fundus images using generative adversarial networks. *arXiv preprint arXiv:2007.09191*, 2020. 2, 7
- [27] Sharif Amit Kamran, Khondker Fariha Hossain, Alireza Tavakkoli, and Stewart Lee Zuckerbrod. Fundus2angio: A novel conditional gan architecture for generating fluorescein angiography images from retinal fundus photography. *arXiv preprint arXiv:2005.05267*, 2020. 2, 7
- [28] Sharif Amit Kamran, Sourajit Saha, Ali Shihab Sabbir, and Alireza Tavakkoli. Optic-net: A novel convolutional neural network for diagnosis of retinal diseases from optical tomography images. In *2019 18th IEEE International Conference On Machine Learning And Applications (ICMLA)*, pages 964–971. IEEE, 2019. 1
- [29] Sharif Amit Kamran, Alireza Tavakkoli, and Stewart Lee Zuckerbrod. Improving robustness using joint attention network for detecting retinal degeneration from optical coherence tomography images. In *2020 IEEE International Conference On Image Processing (ICIP)*, pages 2476–2480. IEEE, 2020. 1

- [30] Salman Khan, Muzammal Naseer, Munawar Hayat, Syed Waqas Zamir, Fahad Shahbaz Khan, and Mubarak Shah. Transformers in vision: A survey. *arXiv preprint arXiv:2101.01169*, 2021. [2](#)
- [31] Junho Kim, Minjae Kim, Hyeonwoo Kang, and Kwanghee Lee. U-gat-it: unsupervised generative attentional networks with adaptive layer-instance normalization for image-to-image translation. *arXiv preprint arXiv:1907.10830*, 2019. [2](#), [7](#)
- [32] Diederik P Kingma and Jimmy Ba. Adam: A method for stochastic optimization. *arXiv preprint arXiv:1412.6980*, 2014. [6](#)
- [33] Anthony SL Kwan, Chris Barry, Ian L McAllister, and Ian Constable. Fluorescein angiography and adverse drug reactions revisited: the lions eye experience. *Clinical & experimental ophthalmology*, 34(1):33–38, 2006. [1](#)
- [34] Kris A Kwiterovich, Maureen G Maguire, Robert P Murphy, Andrew P Schachat, Neil M Bressler, Susan B Bressler, and Stuart L Fine. Frequency of adverse systemic reactions after fluorescein angiography: results of a prospective study. *Ophthalmology*, 98(7):1139–1142, 1991. [1](#)
- [35] Chuan Li and Michael Wand. Precomputed real-time texture synthesis with markovian generative adversarial networks. In *European conference on computer vision*, pages 702–716. Springer, 2016. [2](#), [4](#)
- [36] Henry H Li, Joseph R Abraham, Duriye Damla Sevgi, Sunil K Srivastava, Jenna M Hach, Jon Whitney, Amit Vasanji, Jamie L Reese, and Justis P Ehlers. Automated quality assessment and image selection of ultra-widefield fluorescein angiography images through deep learning. *Translational Vision Science & Technology*, 9(2):52–52, 2020. [1](#)
- [37] Jae Hyun Lim and Jong Chul Ye. Geometric gan. *arXiv preprint arXiv:1705.02894*, 2017. [5](#), [6](#)
- [38] Rodrigo Pessoa Cavalcanti Lira, Cleriston Lucena de Andrade Oliveira, Marta Virgínia Ribeiro Brito Marques, Alaine Rocha Silva, and Cristiano de Carvalho Pessoa. Adverse reactions of fluorescein angiography: a prospective study. *Arquivos brasileiros de oftalmologia*, 70(4):615–618, 2007. [1](#)
- [39] NARESH Mandava, ELIAS Reichel, D Guyer, et al. Fluorescein and icg angiography. *St Louis: Mosby*, 106:800–808, 2004. [1](#)
- [40] Viola Stella Mary, Elijah Blessing Rajasingh, and Ganesh R Naik. Retinal fundus image analysis for diagnosis of glaucoma: a comprehensive survey. *IEEE Access*, 2016. [1](#)
- [41] Dong Nie, Roger Trullo, Jun Lian, Caroline Petitjean, Su Ruan, Qian Wang, and Dinggang Shen. Medical image synthesis with context-aware generative adversarial networks. In *International conference on medical image computing and computer-assisted intervention*, pages 417–425. Springer, 2017. [2](#)
- [42] Dong Nie, Roger Trullo, Jun Lian, Li Wang, Caroline Petitjean, Su Ruan, Qian Wang, and Dinggang Shen. Medical image synthesis with deep convolutional adversarial networks. *IEEE Transactions on Biomedical Engineering*, 65(12):2720–2730, 2018. [2](#)
- [43] Xiangji Pan, Kai Jin, Jing Cao, Zhifang Liu, Jian Wu, Kun You, Yifei Lu, Yufeng Xu, Zhaoan Su, Jiekai Jiang, et al. Multi-label classification of retinal lesions in diabetic retinopathy for automatic analysis of fundus fluorescein angiography based on deep learning. *Graefes Archive for Clinical and Experimental Ophthalmology*, 258(4):779–785, 2020. [1](#)
- [44] Taesung Park, Ming-Yu Liu, Ting-Chun Wang, and Jun-Yan Zhu. Semantic image synthesis with spatially-adaptive normalization. In *Proceedings of the IEEE Conference on Computer Vision and Pattern Recognition*, pages 2337–2346, 2019. [3](#)
- [45] Ryan Poplin, Avinash V Varadarajan, Katy Blumer, Yun Liu, Michael V McConnell, Greg S Corrado, Lily Peng, and Dale R Webster. Prediction of cardiovascular risk factors from retinal fundus photographs via deep learning. *Nature Biomedical Engineering*, 2(3):158, 2018. [1](#)
- [46] Olaf Ronneberger, Philipp Fischer, and Thomas Brox. U-net: Convolutional networks for biomedical image segmentation. In *International Conference on Medical image computing and computer-assisted intervention*, pages 234–241. Springer, 2015. [1](#)
- [47] Patsorn Sangkloy, Jingwan Lu, Chen Fang, Fisher Yu, and James Hays. Scribbler: Controlling deep image synthesis with sketch and color. In *Proceedings of the IEEE Conference on Computer Vision and Pattern Recognition*, pages 5400–5409, 2017. [2](#)
- [48] Tamar Rott Shaham, Tali Dekel, and Tomer Michaeli. Singan: Learning a generative model from a single natural image. In *Proceedings of the IEEE International Conference on Computer Vision*, pages 4570–4580, 2019. [3](#)
- [49] Hoo-Chang Shin, Neil A Tenenholz, Jameson K Rogers, Christopher G Schwarz, Matthew L Senjem, Jeffrey L Gunter, Katherine P Andriole, and Mark Michalski. Medical image synthesis for data augmentation and anonymization using generative adversarial networks. In *International workshop on simulation and synthesis in medical imaging*, pages 1–11. Springer, 2018. [2](#)
- [50] Karen Simonyan and Andrew Zisserman. Very deep convolutional networks for large-scale image recognition. *arXiv preprint arXiv:1409.1556*, 2014. [5](#)
- [51] Alireza Tavakkoli, Sharif Amit Kamran, Khondker Fariha Hossain, and Stewart Lee Zuckerbrod. A novel deep learning conditional generative adversarial network for producing angiography images from retinal fundus photographs. *Scientific Reports*, 10(1):1–15, 2020. [2](#)
- [52] Ashish Vaswani, Noam Shazeer, Niki Parmar, Jakob Uszkoreit, Llion Jones, Aidan N Gomez, Lukasz Kaiser, and Illia Polosukhin. Attention is all you need. In *NIPS*, 2017. [2](#)
- [53] Abdul Waheed, Muskan Goyal, Deepak Gupta, Ashish Khanna, Fadi Al-Turjman, and Plácido Rogerio Pinheiro. Covidgan: data augmentation using auxiliary classifier gan for improved covid-19 detection. *Ieee Access*, 8:91916–91923, 2020. [2](#)
- [54] Ting-Chun Wang, Ming-Yu Liu, Jun-Yan Zhu, Andrew Tao, Jan Kautz, and Bryan Catanzaro. High-resolution image synthesis and semantic manipulation with conditional gans. In *Proceedings of the IEEE conference on computer vision and pattern recognition*, pages 8798–8807, 2018. [2](#), [3](#), [5](#), [7](#)

- [55] Wenqi Xian, Patsorn Sangkloy, Varun Agrawal, Amit Raj, Jingwan Lu, Chen Fang, Fisher Yu, and James Hays. Texturegan: Controlling deep image synthesis with texture patches. In *Proceedings of the IEEE Conference on Computer Vision and Pattern Recognition*, pages 8456–8465, 2018. [2](#)
- [56] Han Zhang, Ian Goodfellow, Dimitris Metaxas, and Augustus Odena. Self-attention generative adversarial networks. In *International Conference on Machine Learning*, pages 7354–7363, 2019. [4](#), [5](#), [6](#)
- [57] Han Zhang, Tao Xu, Hongsheng Li, Shaoting Zhang, Xiaogang Wang, Xiaolei Huang, and Dimitris N Metaxas. Stackgan: Text to photo-realistic image synthesis with stacked generative adversarial networks. In *Proceedings of the IEEE international conference on computer vision*, pages 5907–5915, 2017. [2](#)
- [58] Jun-Yan Zhu, Philipp Krähenbühl, Eli Shechtman, and Alexei A Efros. Generative visual manipulation on the natural image manifold. In *European Conference on Computer Vision*, pages 597–613. Springer, 2016. [2](#)